SCIEPublish

Article

Catalytic Potential of Green-Synthesized Iron Nanoparticles from *Psidium guajava* for 4-Nitrophenol Reduction

Filipe Kalil da Silva Naves [1], Yasmin Milena Loth Bueno [1], Marcus André Cardoso de Araujo [1], Giane Gonçalves Lenzi [2], Rodrigo Brackmann [1,*] and Marcio Barreto Rodrigues [1]

[1] Programa de Pós-Graduação em Tecnologia de Processos Químicos e Bioquímicos (PPGTP), Universidade Tecnológica Federal do Paraná (UTFPR), Via do Conhecimento, s/n, km 01, Pato Branco 85503-390, Paraná, Brazil; filipenaves@alunos.utfpr.edu.br (F.K.d.S.N.); yasminbueno@alunos.utfpr.edu.br (Y.M.L.B.); maraujo@alunos.utfpr.edu.br (M.A.C.d.A.); marciorodrigues@utfpr.edu.br (M.B.R.)

[2] Departamento de Engenharia Química, Universidade Tecnológica Federal do Paraná (UTFPR), Av Monteiro Lobato, s/n, Km 04, Ponta Grossa 84016-210, Paraná, Brazil; gianeg@utfpr.edu.br (G.G.L.)

* Corresponding author. E-mail: rodrigobrackmann@utfpr.edu.br (R.B.)

Received: 12 August 2025; Accepted: 18 September 2025; Available online: 11 October 2025

ABSTRACT: This study presents a sustainable approach for the green synthesis of iron nanoparticles (Fe(NPs)) using an aqueous extract of *Psidium guajava* (guava leaves) as a reducing and stabilizing agent. The FeNPs were applied in the catalytic reduction of 4-nitrophenol. To minimize the use of sodium borohydride ($NaBH_4$), different volumetric ratios of plant extract and $NaBH_4$ were tested. The influence of these ratios on the physicochemical and morphological properties of the FeNPs was evaluated using X-ray diffraction (XRD), scanning electron microscopy with energy-dispersive X-ray spectroscopy (SEM/EDS), high-resolution field-emission SEM (HR-FESEM), Fourier-transform infrared spectroscopy (FTIR), thermogravimetric analysis (TGA), and N_2 physisorption. Increasing the proportion of plant extract led to reduced crystallinity, larger particle sizes, and lower surface areas. Despite these changes, using up to 40% extract improved catalytic performance, achieving over 90% reduction of 4-nitrophenol. Ecotoxicological assessments confirmed the biocompatibility of the FeNPs, the effective neutralization of 4-nitrophenol toxicity post-reduction, and highlighted the inherent toxicity of $NaBH_4$. These findings demonstrate the potential of *Psidium guajava*-mediated FeNPs as eco-friendly catalysts for pollutant reduction, combining efficiency with reduced environmental impact.

Keywords: Iron oxides; Stabilization; Vegetable coating; Sodium borohydride; Ecotoxicological tests

1. Introduction

The green synthesis of iron nanoparticles (Fe(NPs)) represents a promising research area that has attracted increasing scientific interest, particularly over the last decade, due to its environmental relevance. This innovative approach combines the principles of green chemistry with nanotechnology, aiming at the production of iron-based materials at the nanoscale with various environmentally beneficial applications [1], such as wastewater treatment [2], contaminant remediation [3], and heterogeneous catalysis [4]. Furthermore, Fe(NPs) may exhibit magnetic properties that further enhance their versatility in catalytic applications, facilitating their recovery and reuse—an excellent advantage compared to nanoparticles synthesized from other metals [5].

Despite the growing interest in green synthesis, conventional synthesis methods, whether physical or chemical, are still widely employed. Physical techniques, such as laser ablation and milling, rely on mechanical force or energy to reduce the size of larger particles; however, they are generally associated with high costs and limited control over morphology and particle size [6]. In contrast, chemical approaches, such as coprecipitation, employ reducing agents—most notably sodium borohydride ($NaBH_4$) and cetyltrimethylammonium bromide ($C_{19}H_{42}BrN$)—often in combination with stabilizing compounds to prevent the formation of undesirable agglomerates, which compromise the surface area and reactivity of Fe(NPs) [1].

https://doi.org/10.70322/gct.2025.10018

However, these conventional methods present significant drawbacks. They require stringent operating conditions (pressure, excessive energy input, inert atmosphere, and high temperatures) and generate toxic byproducts that undermine the process's sustainability and economic feasibility. Moreover, the demand for high-purity reagents and synthetic stabilizers further increases costs and environmental impact [7,8].

In this context, green synthesis emerges as a promising alternative. Several studies have already demonstrated its feasibility by employing plant extracts as reducing and stabilizing agents. For instance, synthesis can be done using parts of the plant *Daucus carota* subsp. *Sativus* has shown the ability to convert iron salts into nanoparticles with applications in Fenton-type processes [9]. Similarly, iron nanoparticles anchored on carbon dots derived from lemon peel (LP-CDs@Fe_3O_4) have been reported for photocatalysis [10]. Another study describes the synthesis of bimetallic Ag-Fe nanoparticles from *Calyptocarpus vialis* extract, which exhibited excellent performance in the catalytic reduction of 4-nitrophenol [8].

The synthesis of nanoparticles based on the principles of green chemistry constitutes a promising approach, as it combines enhanced operational safety with the minimization of toxic waste generation, thereby reducing potential environmental liabilities. Furthermore, it demonstrates high compatibility with sustainability strategies and economic efficiency, unlike conventional methods that rely on more aggressive synthetic routes [11].

Green synthesis routes employ environmentally benign reagents and procedures with the aim of reducing waste generation, toxicity, energy consumption, and the use of non-renewable resources, thereby promoting greater environmental sustainability in the production of iron nanoparticles [11]. Among the materials used, aqueous plant extracts stand out, acting simultaneously as reducing and stabilizing agents. This occurs due to the presence of active chemical species such as terpenes, flavonoids, phenols, and reducing sugars, among others. Initially, the extract promotes the reduction of the metal ion and subsequently forms a coating on the nanoparticle surface, preventing rapid passivation and agglomeration [12]. Several plants have been reported effective in this context, with different parts—roots, stems, flowers, fruits, and leaves—applicable in green synthesis protocols [9,12].

However, despite its numerous advantages, the main limitations of this approach are restricted morphological control and lower catalytic performance when compared to nanoparticles obtained through conventional chemical methods. The inherent variability of plant extracts and the lower reducing efficiency of their active compounds often result in nanoparticles with low crystallinity, heterogeneous particle size, and a tendency toward agglomeration [13]. These factors directly compromise the surface area and catalytic reactivity of the nanoparticles, creating a research gap in the pursuit of strategies that combine the sustainability of green synthesis with the efficiency and morphological control of traditional methods.

The objective of this study was the green synthesis and characterization of iron nanoparticles using an aqueous extract of guava leaves (*Psidium guajava*). Guava leaves were chosen based on their composition, rich in potentially reducing and stabilizing compounds [14]. An innovative aspect of this research was the combination of the plant extract with a conventional reducing agent ($NaBH_4$) to evaluate how different proportions of these agents could impact the crystallinity, particle size, morphology, and reactivity of the Fe(NPs). Another notable feature of the study was the use of a simple, low-cost synthesis process that does not require expensive equipment, reagents, or reaction conditions, allowing easy reproducibility of the synthesis method while producing Fe(NPs) with excellent catalytic performance in the reduction of 4-nitrophenol to 4-aminophenol.

2. Materials and Methods

2.1. Aqueous Plant Extract

The aqueous extraction was conducted following the procedure outlined by Samari et al. with modifications [15]. *Psidium guajava* leaves were washed with distilled water, air-dried in the shade at room temperature, and subsequently ground using a knife mill (Willey-type, SL-31, Solab científica, São Paulo, Brazil) operated at 5000 rpm for 10 min until a homogeneous fine powder with particle size below 200 μm was obtained. Subsequently, 10 g of guava leaf powder was mixed with 100 mL of distilled water in a 500 mL Erlenmeyer flask. The mixture was stirred continuously at 400 rpm using a magnetic stirrer (Fisatom 752A, 7lab, São Paulo, Brazil) and maintained at 80 °C for 15 min. Afterwards, the extract was filtered using Whatman No. 1 filter paper and used immediately.

2.2. Determining Antioxidant Activity by Reducing the Ferric Reducing Antioxidant Power (FRAP) Assay

The ferric reducing antioxidant power (FRAP) method is based on the direct measurement of the ability of antioxidants (reducing agents) in the sample to reduce, under acidic conditions (pH 3.6), the Fe^{3+}/tripyridyltriazine

(TPTZ) complex to Fe^{2+}, which exhibits an intense blue color with maximum absorption at 595 nm. Initially, solutions of hydrochloric acid (HCl) 40 mmol L^{-1}, acetate buffer 0.3 mol L^{-1} at pH 3.6 ($C_2H_3NaO_2$), TPTZ solution 10 mmol L^{-1} (2,4,6-tris(2-pyridyl)-s-triazine), and ferric chloride solution 20 mmol L^{-1} ($FeCl_3$) were prepared. These solutions were then used to prepare the FRAP reagent by mixing 25 mL of acetate buffer with 2.5 mL of TPTZ solution and 2.5 mL of aqueous ferric chloride solution. The procedure involves mixing 100 µL of the sample with 3 mL of FRAP reagent. The mixture was homogenized using a vortex mixer (ION, VX-28-BI, Prolab, Brazil) operated at 2500 rpm for 1 min and then incubated in a water bath at 37 °C for 30 min, protected from light. Finally, absorbance was measured at 595 nm using a Lambda 45 spectrophotometer (Perkin Elmer, Shelton, CT, USA). A freshly prepared calibration curve using ferrous sulfate (200 to 2000 µmol L^{-1}) was used to calculate the antioxidant activity of the extract.

2.3. Green Synthesis of the Iron Nanoparticles (Fe(NPs))

In the procedure, solutions of 0.2 mol L^{-1} sodium borohydride ($NaBH_4$), 0.05 mol L^{-1} ferric chloride hexahydrate ($FeCl_3 \cdot 6H_2O$), and 0.05 mol L^{-1} ferrous sulfate heptahydrate ($FeSO_4 \cdot 7H_2O$) were prepared. In addition, the previously obtained aqueous extract, with a concentration of 100 g L^{-1}, was employed. For the reaction medium, a 1.5 L beaker was used, into which the precursor iron solution ($FeCl_3 \cdot 6H_2O$ + $FeSO_4 \cdot 7H_2O$) was added in a 1:1 volume ratio, totaling 500 mL, under constant stirring at 400 rpm using a magnetic stirrer. A dropwise addition system was set up over the precursor iron solution for $NaBH_4$ and/or the extract, with an approximate rate of 0.2 mL s^{-1}. First, the $NaBH_4$ solution was added dropwise; after 5 min of completion, the plant extract was added dropwise. The beaker was sealed with plastic film throughout the synthesis to minimize atmospheric interference in the reaction. After the dropwise addition, the mixture was kept under stirring for an additional 30 min. The resulting black solid products were separated from the reaction medium by vacuum filtration, thoroughly washed with distilled water, and stored in a dry box for subsequent characterization [13].

The synthesized nanoparticles were obtained under the following $NaBH_4$-to-extract ratios: (i) $NaBH_4$ and plant extract 1:1 (*v*/*v*), (ii) $NaBH_4$ and extract 1:4 (*v*/*v*), and (iii) extract solution only (without $NaBH_4$). The iron nanoparticles were designated according to the final concentration of plant extract used and named Fe(NPs) 25%, Fe(NPs) 40%, and Fe(NPs) 50%, respectively. The syntheses of the iron nanoparticles were performed in triplicate.

The Fe(NPs) synthesized using the aqueous extract of guava leaves will be compared with the Fe(NPs) 0%, which were synthesized solely using the reducing agent $NaBH_4$, as reported in previous studies [13].

2.4. Characterizations of Iron Nanoparticles (Fe(NPs))

Different analytical techniques were employed to evaluate how varying proportions of reducing agents influence the characteristics of Fe(NPs).

X-ray Diffraction (XRD) patterns were recorded using a Miniflex 600 instrument (Rigaku, Tokyo, Japan) operating in step mode over a 2θ range of 10–90°, with a step size of 0.02° and a step time of 0.2 s.

Fourier Transform Infrared (FTIR) spectra were obtained using a Frontier spectrometer (Perkin Elmer®, Waltham, MA, USA) equipped with an ATR accessory. Measurements were recorded in the spectral range of 400–4000 cm^{-1} at a resolution of 4 cm^{-1}, accumulating 32 scans per spectrum.

Scanning Electron Microscopy (SEM) images were acquired using a Tescan Vega3 instrument with a Quorum SC7620 sputter coater, coupled with an energy-dispersive X-ray spectroscopy detector (EDS) (Oxford x-Act, Abingdon, UK). Additionally, a detailed morphological investigation was performed by high-resolution field emission scanning electron microscopy (HR-FESEM) using a Tescan Mira3 instrument (Tescan Orsay Holding, Brno, Czech Republic).

Thermogravimetric Analysis (TGA) was performed on an SDT Q600 thermogravimetric analyzer (TA Instruments, New Castle, DE, USA) under a synthetic air flow of 50 mL min^{-1}. The temperature range was ramped from 25 to 1000 °C at a heating rate of 10 °C min^{-1}. The analysis aimed to assess the thermal behavior of Fe(NPs), including determining the temperature range associated with the decomposition of organic components potentially coating the nanoparticles, and to quantify the iron content in the materials.

Surface area and porosity were analyzed using a Quantachrome NOVA gas sorption system, employing N_2 adsorption-desorption measurements carried out at −196 °C for 6 h over a relative pressure (P/P_o) range of 0.02 to 0.95, and the specific surface area was calculated according to the Brunauer-Emmett-Teller (BET) theory.

2.5. Catalytic Reduction

The 4-nitrophenol assay was performed following the methodology described by Sravanthi (2019) with modifications to assess the catalytic activity of the nanoparticles synthesised using the plant extract. In this analysis, 4-nitrophenol is expected to be reduced to 4-aminophenol, a compound that is 233 times less toxic [16]. The reaction progress was monitored by Molecular Absorption Spectroscopy (UV-Vis). In this step, 40 mg of nanoparticles were mixed with 100 mL of an aqueous 4-nitrophenol solution in a 250 mL beaker. The mixture was stirred under vigorous agitation at 600 rpm for 2 min on a magnetic stirrer, and the temperature was maintained constant at 50 °C throughout the process. Subsequently, 50 mL of an aqueous 0.2 mol L^{-1} sodium borohydride solution was added to the mixture, with stirring continued until the solution was decolorized. Sodium borohydride acts as a reducing agent and alkalinizes the reaction medium, converting 4-nitrophenol to 4-nitrophenolate, a species more susceptible to catalytic reduction. The initial concentration of 4-nitrophenol in the tests was 10 mg L^{-1}. During the reduction process, 3 mL aliquots were withdrawn at 2-min intervals. Subsequently, the aliquots were filtered through a membrane filter to remove the catalyst. Finally, the concentration of 4-nitrophenolate was determined at 400 nm by UV-Vis spectroscopy [17].

2.6. Ecotoxicological Tests

Ecotoxicological tests were used as a complementary approach to assess the toxicity of 4-nitrophenol before and after catalytic reduction, focusing on selected trophic levels. Leachates from both uncoated and coated Fe(NPs) were also evaluated. In addition, the chemical agent $NaBH_4$ was assessed to verify its toxicity and highlight the importance of minimizing or replacing its use in synthesis processes.

An acute toxicity assay was conducted using microcrustaceans (brine shrimp) as the test organisms. Glassware was thoroughly washed with water and detergent, then cleaned with 70% ethanol to eliminate potential contaminants. The culture medium (Meyer's Medium) was prepared by dissolving 23 g of sodium chloride (NaCl), 11 g of hexahydrated magnesium chloride ($MgCl{\cdot}6H_2O$), 4 g of sodium sulfate (Na_2SO_4), 1.3 g of calcium chloride ($CaCl_2$), and 0.7 g of potassium chloride (KCl) in 1 L of distilled water. The pH of both the culture medium and test solutions (4-nitrophenol before and after catalytic reduction, Fe(NPs) leachates, and $NaBH_4$) was adjusted to 9. For the hatching process, cysts were placed in Meyer's solution for 48 h under continuous illumination at 28 °C with aeration. After hatching, 10 nauplii were transferred to each well, and 10 mL of the sample was added. The wells were exposed to continuous light at 28 °C for 24 to 48 h. Finally, mortality and immobilization of individuals were recorded at the end of the exposure period. The following treatments were evaluated: 4-nitrophenol at 10 mg L^{-1} (4NF), the last aliquot from the catalytic reduction using Fe(NPs) 25%, leachates from Fe(NPs) 0% and Fe(NPs) 25%, a solution of $NaBH_4$ 0.2 mol L^{-1}, and a blank control (Br) consisting of Meyer's medium only.

The second test was a chronic assay conducted on aquatic plants at the trophic level. Before the assay, all glassware was thoroughly washed with water and detergent, then cleaned with 70% ethenol. The pH of the tested samples—including 4-nitrophenol (before and after catalytic reduction), leachates from Fe(NPs), and $NaBH_4$—was adjusted to 7.5. Each culture well was filled with 10 mL of the sample solution and received 10 fronds. The samples were maintained under continuous illumination at 18–22 °C for 7 days. Finally, cloning and dry mass analysis were performed. The materials tested included: 4-nitrophenol at 10 mg L^{-1} (4NF), the last aliquot from the catalytic reduction using Fe(NPs) 40%, leachates from Fe(NPs) 0% and Fe(NPs) 25%, a solution of $NaBH_4$ 0.2 mol L^{-1}, and a blank control (Br) consisting solely of distilled water.

3. Results and Discussion

3.1. Characterization of the Plant Extract

The extract exhibited a reducing capacity of 116.28 mmol g^{-1} (equivalent to 0.116 mol g^{-1}), indicating its potential for effective iron reduction and applicability in green synthesis approaches methods. Compared to the literature, Cerio et al. prepared an aqueous extract of guava leaves using ultrasound and infusion. In their study, ultrasound extraction proved more efficient, yielding 3026.7 mol g^{-1}, whereas infusion extractions produced values ranging from 314.2 to 285.7 mol g^{-1}. This high reducing capacity can be attributed to the effective extraction procedure, involving the evaporation of the extract followed by dissolution in 50% methanol [18]. Overall, the reducing capacity observed in this study was lower than the values reported in the literature. Differences in extraction methods, the plant species analyzed, and environmental factors such as harvest season, geographic location, and time of year—among other characteristics—can explain such variations.

3.2. X-ray Diffraction (XRD)

Initially, for comparative evaluation, the XRD results obtained for Fe(NPs) 0%, as reported in previous studies, will be highlighted [13]. In this sample, characteristic peaks corresponding to magnetite (Fe_3O_4, JCPDS75-1609) with a cubic structure, lepidocrocite (FeO(OH), JCPDS44-1415), and iron hydroxide oxide (FeO(OH), JCPDS26-0792), both with orthorhombic structures, were identified. This analysis of the Fe(NPs) 0% sample allowed us to assess whether using different volumetric ratios of extracts induced changes in the composition and crystallinity of the nanoparticles [13,19,20].

Figure 1 presents the diffractograms of samples synthesized using guava extract as a coating agent. The Fe(NPs) 25% sample exhibits characteristic diffraction peaks of lepidocrocite (FeO(OH), JCPDS44-1415), with an orthorhombic crystal structure. In contrast, the Fe(NPs) 40% and Fe(NPs) 50% samples exhibited amorphous behavior. The reduction in the crystallinity of the samples is attributed to the presence of bioactive compounds from the extract, which, in higher proportions, interfered with the crystallization process. These compounds may be adsorbed onto the surface of the growing Fe(NPs), hindering the ordered arrangement of atoms, a fundamental condition for achieving high crystallinity [21]. A comparison between the Fe(NPs) 25% and Fe(NPs) 0% samples shows that both exhibit characteristic peaks of lepidocrocite. However, magnetite and iron hydroxide oxide peaks observed in the uncoated Fe(NPs) 0% sample are absent in the Fe(NPs) 25%. This modification is attributed to the distinct roles of the reducing agents during synthesis. In the Fe(NPs) 0% sample, the reduction of iron ions occurs exclusively through $NaBH_4$, which provides a highly reducing environment and does not involve interference from organic molecules in the nucleation and crystal growth process, thus favoring the formation of well-defined phases. In contrast, in the Fe(NPs) 25% sample, the presence of the extract during synthesis contributes to the establishment of a milder reducing environment, in which the organic compounds interfere with crystalline phases formation by altering the reduction and nucleation rates, thereby limiting crystal growth and consequently the formation of well-defined phases [13,19,20].

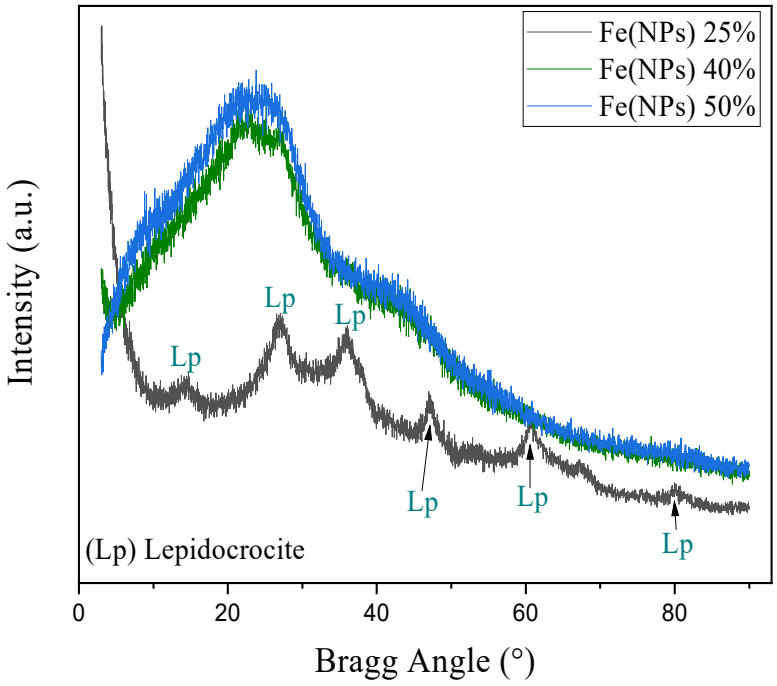

Figure 1. X-ray diffractograms of Fe(NPs) samples synthesized with varying volumetric proportions of plant extract.

Additionally, catalytic reduction tests were performed to evaluate whether these structural differences led to changes in the catalytic activity of the Fe(NPs).

Studies describing similar synthesis methodologies, involving the use of plant extracts under oxygenated atmospheres, also report the tendency for the formation of iron oxides and hydroxides. This phenomenon is mainly attributed to the oxygen-rich atmosphere, which promotes the oxidation of iron ions and favors the formation of these phases. Another factor contributing to the formation of the identified oxides and hydroxides is the absence of thermal treatments during the syntheses [22,23]. In this context, Adhikari et al. (2022) employed a similar synthesis process using *Psidium guajava* leaf extract and sodium hydroxide (NaOH). During their analysis, iron oxides (FeO and Fe_3O_4) and iron hydroxide (FeOH) were identified in the synthesized material [23].

Furthermore, the predominant phase of lepidocrocite is characterized by a monoclinic crystalline structure in which iron ions (Fe), arranged octahedrally, form layers intercalated with hydroxyl groups (OH). The formation of lepidocrocite is frequently reported in the literature as a product of the aging of zero-valent iron nanoparticles (Fe(NPs)), observed after periods of days or months. This phenomenon is attributed to the high reactivity of the material, even upon exposure to atmospheric conditions [19]. Consequently, zero-valent Fe(NPs) require specific conditions, such as an inert nitrogen atmosphere, during the preparation process. This approach minimizes the incorporation of atmospheric gases into the nanoparticles, thereby preventing the formation of oxides and hydroxides during synthesis [24].

3.3. Fourier Transform Infrared Spectroscopy (FTIR)

Infrared analysis was employed to evaluate the effectiveness of the vegetal coating from the plant extract, specifically to determine whether compounds present in the extract matrix could interact with the surface of Fe(NPs) and stabilize them. Figure 2 presents the FTIR spectra of the guava extract-coated Fe(NPs).

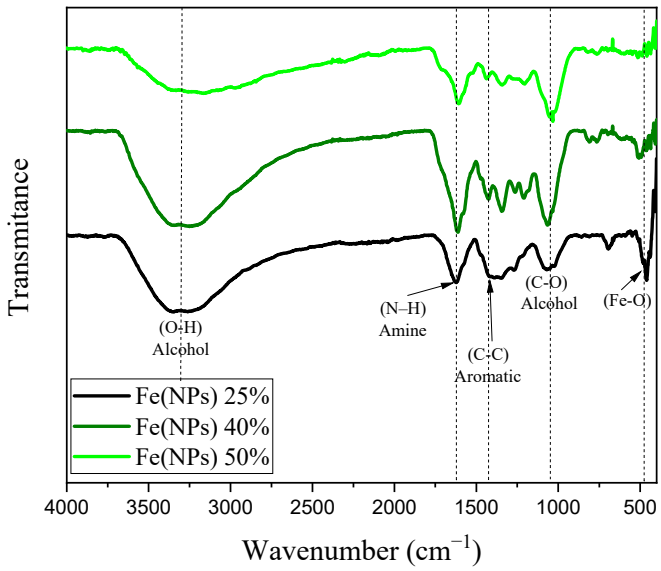

Figure 2. FTIR spectra of Fe(NPs) coated with guava leaf extract.

In this context, Table 1 summarizes the infrared absorption bands observed in Fe(NPs) coated with guava extract.

Table 1. Characteristic FTIR bands observed in Fe(NPs) coated with guava extract.

Bands	Wavenumber (cm^{-1})	Groups
Fe-O	470–600	Inorganic portion
Vibration of (C-O)	900–1200	Alcohol
Bond (C-C)	1400	Aromatic compounds (phenols)
N-H	1645	Amine
Stretching (O-H)	3340	Alcohol

The FTIR spectra of the coated samples exhibit characteristic bands of the Fe-O bond between 470 and 600 cm^{-1} [23,25], with significant shifts likely associated with the organic components of the guava extract. These Fe-O shifts occur due to the formation of distinct iron phases, as confirmed by XRD analysis. Additionally, the spectra of the coated samples show an intense band between 900 and 1200 cm^{-1}, attributed to the C-O vibration of alcohols [14]. The band at 1400 cm^{-1} corresponds to the C-C bond in aromatic compounds (phenols) [26], while the band at 1645 cm^{-1} is likely related to the N-H bond of amines [14]. A broad band near 3340 cm^{-1} observed in the coated samples is associated with the O-H stretching vibration of alcohols [14,23]. These findings indicate that the vegetal coating with the organic matrix effectively promotes stabilization through the presence of alcohols, aromatic compounds, and amines.

Similarly, studies employing the green synthesis of iron nanoparticles reveal the presence of the aforementioned bands, either associated with the same functional groups previously highlighted or with other functional groups, depending on the use of different plant extracts or distinct extraction methods. For instance, in a study that utilized *Psidium guajava* leaf extract for the green synthesis of iron nanoparticles, an intense band was again observed around 3340 cm^{-1}, attributed to the O-H stretching vibration of alcohols and phenols. The band near 1680 cm^{-1} was assigned to the C=O stretching of carbonyl groups in esters, whereas the band at 572 cm^{-1} was attributed to the Fe–O bond [23].

Similarly, in the green synthesis of iron nanoparticles from the aqueous extract of *Ziziphus* leaves, the band near 3340 cm^{-1} was once more observed, assigned to the O-H stretching vibration characteristic of alcohols, flavonoids, and phenols. The region between 900 and 1200 cm^{-1} was associated with C-O stretching, while the band at 1640 cm^{-1} was related to C=O stretching vibration [27].

In all studies, the presence of the band associated with the Fe-O bond was observed, indicating the formation of iron oxides or hydroxides, which XRD analyses can further confirmed. An example is the Fe(NPs) 25% sample, which exhibited peaks characteristic of lepidocrocite.

3.4. Scanning Electron Microscopy (SEM/EDS) and High-Resolution Field Emission Scanning Electron Microscopy (HR-FESEM)

Scanning electron microscopy (SEM) with energy-dispersive X-ray spectroscopy (EDS), as well as high-resolution field emission scanning electron microscopy (HR-FESEM), were employed for the qualitative evaluation of the structures of Fe(NPs). Their distinct magnification capabilities justify the application of both techniques. SEM enabled a comparative analysis of the tendency toward agglomeration and irregular morphologies, whereas HR-FESEM allowed for detailed visualization of surface features such as fissures and pores.

Again, for comparative purposes, the morphological characteristics exhibited by Fe(NPs) 0%, as presented in previous studies, will be discussed [13]. Firstly, at a magnification of 250X, the sample displays irregular particle sizes, which can be associated with the absence of a coating agent. Consequently, the particles tend to agglomerate, leading to size heterogeneity. Additionally, pores are observed at a magnification of 50 kX, suggesting that the material has potential for catalytic activity [13].

Figure 3 presents the SEM and HR-FESEM images of the Fe(NPs) synthesized with different volumetric proportions of plant extract at magnifications of 500X and 80 kX, respectively. At a 500X magnification, the samples exhibit agglomerates of particles of varied sizes. This is attributed to the guava extract containing a diverse range of compounds that can coat and stabilize the nanoparticles, leading to heterogeneous morphologies. Additionally, a qualitative assessment shows that the sample with 25% plant extract (Fe(NPs) 25%) exhibits agglomerates of smaller particles compared to the samples with other extract concentrations. Specifically, synthesizing nanoparticles with volumetric proportions of plant extract exceeding 25% leads to larger agglomerates of particles, potentially influencing catalytic activity and reducing the material's surface area. The N_2 physisorption corroborates this reduction in surface area. Furthermore, at 80 kX magnification, the nanoparticles exhibit fissures or pores, suggesting that the material may serve as an effective adsorbent. Thus, the heterogeneity in the size and morphology of the Fe(NPs) can be attributed to the diversity of compounds present in the plant extract, such as alcohols and aromatic compounds, which act in the coating and stabilization of the materials, as evidenced by the presence of functional groups in the FTIR analysis, thereby conferring structural variation within the same catalyst. Furthermore, using different volumes of the aqueous extract influences the reduction and nucleation rates, promoting significant changes in the morphology and size of the catalytic particles [28,29].

Similarly, the study conducted by Kumari et al. (2023) demonstrated the presence of irregular shapes and a wide size distribution of Fe(NPs) synthesized using plant extracts [28]. Likewise, Mokshith et al. (2022) reported Fe(NPs) exhibiting both spherical and distorted shapes, along with significant size variability [29]. These studies support the notion that the complex matrix of compounds in plant extracts imparts such characteristics to the Fe(NPs) [29]. In the context of nanoparticle synthesis using plant extracts, several factors can be adjusted to control morphological properties, including the concentration of the plant extract, which directly influences the rate of reduction and nucleation.

Energy Dispersive Spectroscopy (EDS) analysis allows for the evaluation of iron ions present in the Fe(NPs), as illustrated in Figure S1. The presence of these ions is confirmed in all samples, which is ideal for ensuring high catalytic performance due to the well-known versatility of iron in catalyzing various reactions and its capacity to form complexes with diverse organic molecules [30]. Additionally, complementary thermal analysis may provide a quantitative

elucidation of the iron ion content, enabling investigation of whether variations in the volumetric proportions of the plant extract lead to changes in iron loading in each sample.

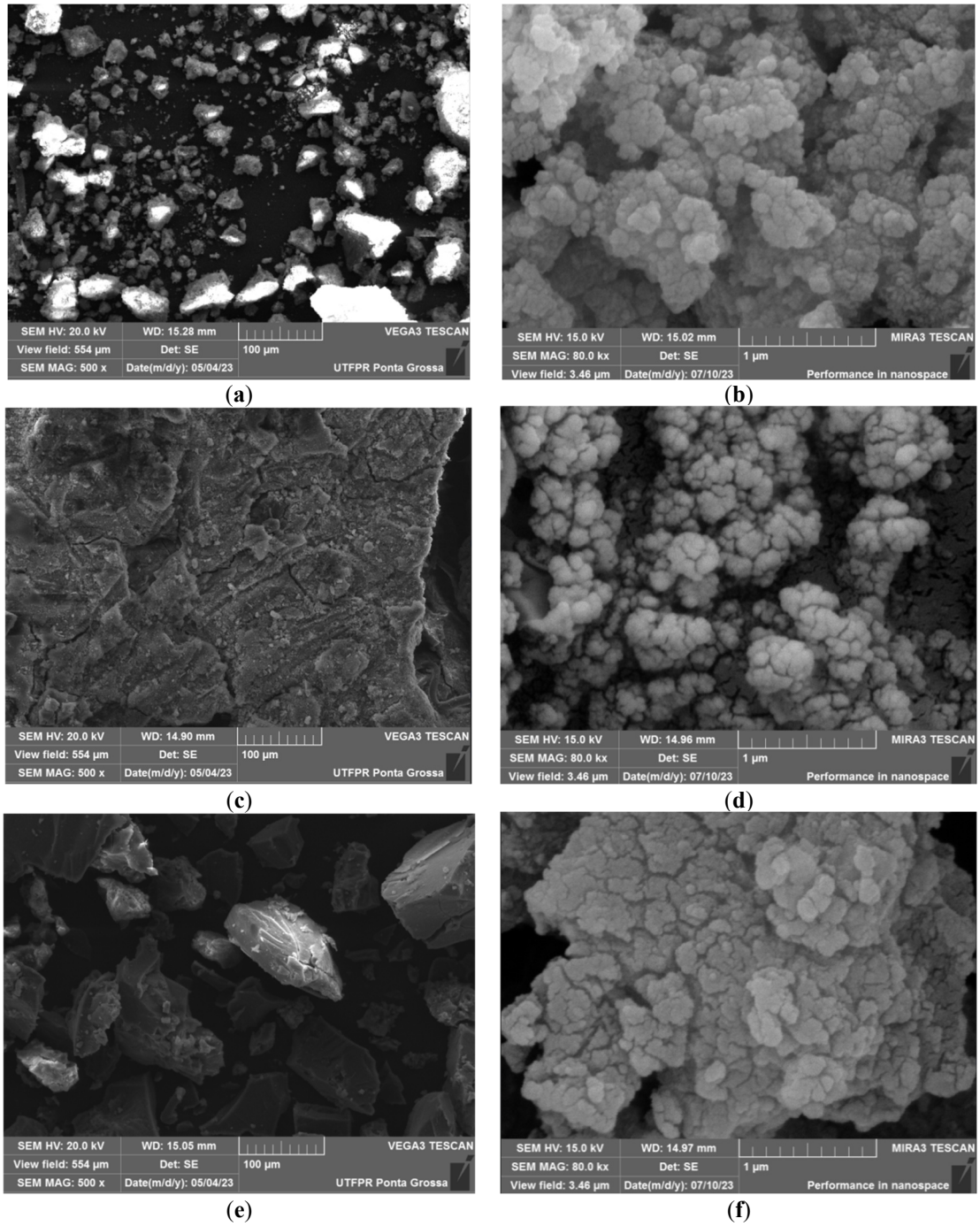

Figure 3. SEM and HR-FESEM images of the coated Fe(NPs) synthesized with different volumetric proportions of plant extract: (**a**) Fe(NPs) 25% at 500X, (**b**) Fe(NPs) 25% at 80 kX, (**c**) Fe(NPs) 40% at 500X, (**d**) Fe(NPs) 40% at 80 kX, (**e**) Fe(NPs) 50% at 500X and (**f**) Fe(NPs) 50% at 80 kX.

3.5. Surface Area and Pore Volume Evaluation

Figure 4 presents the nitrogen adsorption-desorption isotherms of the Fe(NPs). The Fe(NPs) 0% sample, synthesized in previous studies [13], and the Fe(NPs) 40% samples exhibit type IV isotherms with H3-type hysteresis loops, indicating mesoporous structures. These mesoporous isotherms are characterized by slow initial adsorption at low relative pressures, followed by rapid adsorption at higher pressures, suggesting specific interactions between the adsorbate and the internal pore surfaces [13,31,32].

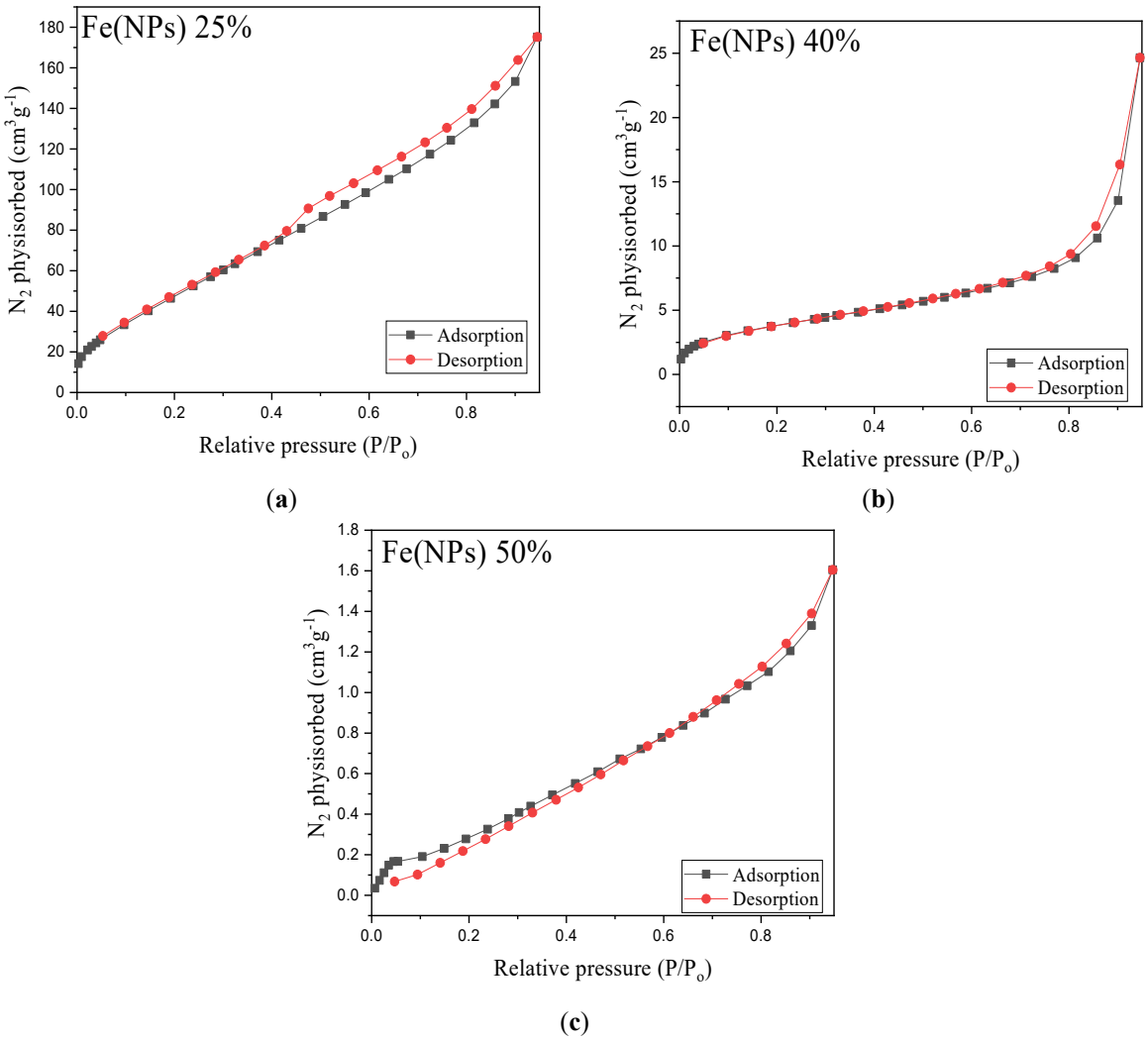

Figure 4. Nitrogen adsorption-desorption isotherms of Fe(NPs) synthesized with different volumetric proportions of plant extract: (**a**) Fe(NPs) 25% (**b**) Fe(NPs) 40% and (**c**) Fe(NPs) 50%.

On the other hand, the samples shown in Figure 4a Fe(NPs) 25% and Figure 4c Fe(NPs) 50% exhibit type III isotherms, characterized by a rapid and continuous accumulation of adsorbed gas on the surface of the solids throughout the entire analyzed pressure range, without a discernible adsorption plateau. This behavior suggests the absence of well-defined multilayers and indicates weak interactions between the adsorbent and adsorbate. The lack of a plateau is typical of porous materials with broad and heterogeneous pore size distributions. Notably, the Fe(NPs) 25% sample also exhibits H3-type hysteresis, suggesting a non-uniform distribution in pore size and shape [31,33].

These findings underscore the complexity and variability of the porous structures of the Fe(NPs) and the dynamics of interactions between the adsorbent and the adsorbate during the adsorption process in each sample.

Figure 5 displays the pore size distributions of the Fe(NPs). The samples synthesized with Fe(NPs) 0% and Fe(NPs) 25% plant extract exhibit similar pore distributions, characterized by a high concentration of pores around 1.8 nm, indicating non-uniformity [13]. In contrast, the Fe(NPs) 40% and Fe(NPs) 50% samples present more uniform pore size distributions, with no significant concentration of pores at similar dimensions.

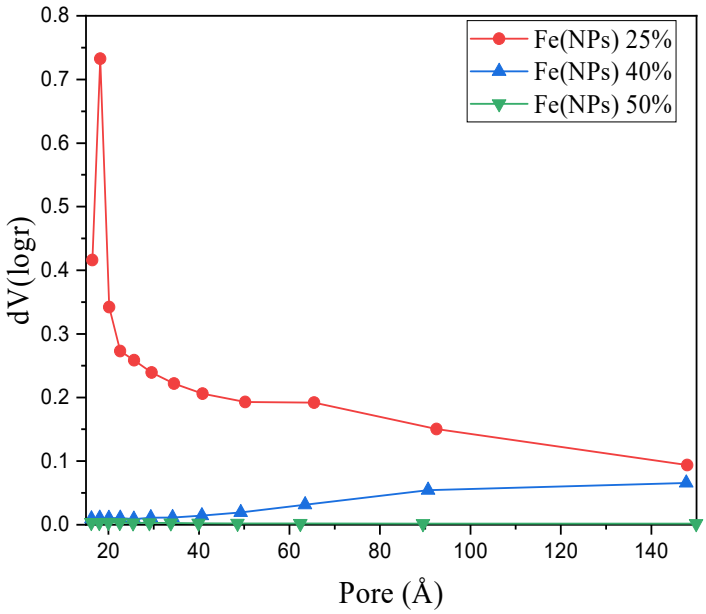

Figure 5. Pore size distributions of the Fe(NPs) samples synthesized with different volumetric proportions of plant extract.

Table 2 presents the textural properties of the Fe(NPs), determined by N_2 physisorption at −196 °C. The Fe(NPs) 25% and Fe(NPs) 0% samples exhibited the highest surface areas and pore volumes [13]. In contrast, the other samples showed notable reductions in surface area, which may negatively impact their catalytic activity. As particle size decreases, the surface area-to-volume ratio increases significantly, leading to a larger surface area relative to volume. This phenomenon imparts distinctive properties and behaviors to nanoparticles compared to their macroscopic particles. Owing to their high surface area, nanoparticles possess an enhanced ability with their environment, which is a key factor behind their wide range of applications and prominence as a study subject in various scientific fields.

Table 2. Textural properties of the Fe(NPs) determined by N_2 physisorption at −196 °C.

Samples	Specific Area ($m^2\ g^{-1}$)	Pore Volume ($cm^3\ g^{-1}$)	Average Pore Size (nm)
Fe(NPs) 25%	204.8	0.200	1.8
Fe(NPs) 40%	14.2	0.040	9.1
Fe(NPs) 50%	1.4	0.002	1.6

The Fe(NPs) 40% and Fe(NPs) 50% samples also exhibited reduced pore volumes compared to the others, with a significant decrease. Pore volume is a critical parameter in various applications, from catalysts to adsorption, as it affects the capacity to store or transport substances within the nanoparticle pores—a factor that greatly influences their properties and functionalities.

Regarding average pore size, the Fe(NPs) 0%, Fe(NPs) 25%, and Fe(NPs) 50% samples exhibited similar values below 2 nm, indicating the predominance of micropore structures [13]. Notably, the Fe(NPs) 50% sample showed a more homogeneous distribution, with a subtle concentration of pores of similar size. In contrast, Fe(NPs) 0% and Fe(NPs) 25% samples presented a high concentration of pores around 1.8 nm [13]. For the Fe(NPs) 40% sample, the average pore size was 9.1 nm, representing a significant increase compared to the others. This sample also exhibited a homogeneous distribution, with a slight concentration of pores of comparable size.

Average pore size, like pore volume, plays a fundamental role in determining the transport characteristics, adsorption behavior, and other physicochemical properties of porous materials. This parameter is particularly important in applications involving the selective adsorption of molecules.

It is worth highlighting that the synthesized Fe(NPs) exhibited considerable variations in surface area and pore volume, a phenomenon also reported in the literature, which arises due to different synthesis methods, types, and amounts of plant extracts employed, among other factors. In this context, iron nanoparticles synthesized using extracts from *Syzygium cumini* seeds, *Punica granatum* peels, *Pisum sativum* peels, *Ridge gourd* peels, and *Calliandra haematocephala* leaves exhibited surface areas of 3.5, 10.9, 17.6, 26.2, and 63.89 $m^2\ g^{-1}$, while the corresponding pore volumes were 0.99, 0.07, 0.04, 0.13, and 0.11 $cm^3\ g^{-1}$, respectively [34]. Moreover, in another study, iron nanoparticles

synthesized via a coprecipitation process using $NaBH_4$ yielded two catalysts with surface areas of 47.5 and 62.5 $m^2\ g^{-1}$, pore volumes of 0.103 and 0.2 $cm^3\ g^{-1}$, and average pore sizes of 9.8 and 14.3 nm, respectively [35]. These findings clearly demonstrate that the textural properties of Fe(NPs) vary significantly depending on the synthesis route and the use of different extracts [34]. In the present study, the variations in textural properties can be ascribed to the different proportions of $NaBH_4$ and plant extract employed during synthesis, which modulate the reaction medium and provide distinct reduction and nucleation rates, thereby leading to different Fe(NPs) characteristics. Finally, it is worth emphasizing the textural properties of the Fe(NPs) 25% sample, which exhibited superior surface area and pore volume compared to values reported in the literature, making it a promising candidate for catalytic applications, with excellent potential as an adsorbent.

3.6. Thermal Analysis

For comparative purposes, the results obtained for Fe(NPs) 0% are again reported, as previously published [13]. Thermogravimetric analysis (TGA) reveals a gradual mass loss of 11.33% from room temperature up to approximately 350 °C, likely associated with hydrogen release from the lepidocrocite and iron hydroxide oxide phases. Upon heating beyond 400 °C, the sample exhibits a mass gain continuing up to 570 °C, reaching 108.4% of the original mass. This increase is attributed to the oxidation of the material to the hematite phase (α-Fe_2O_3). Additionally, the iron content in the sample was calculated to be 7.34 mg [13].

Regarding the differential thermal analysis (DTA), an exothermic signal was detected at approximately 470 °C, which is associated with a mass loss [13].

Figure 6 illustrates the thermal analyses of Fe(NPs) coated with guava plant extract. The samples exhibit mass losses from room temperature up to approximately 400 °C, attributed to the degradation of the organic fraction derived from the plant extract. For the Fe(NPs) 25% sample, the mass loss is less pronounced, approximately 53.13%, possibly due to partial oxidation of the material into hematite (α-Fe_2O_3). In contrast, the Fe(NPs) 40% and Fe(NPs) 50% samples display significantly higher mass losses, at 83.14% and 83.86%, respectively. These results suggest that these materials were already in an oxidized state; therefore, no mass gain occurs due to oxygen incorporation. The iron mass values were calculated as 2.90 mg for Fe(NPs) 25%, 0.96 mg for Fe(NPs) 40%, and 1.01 mg for Fe(NPs) 50% samples.

The mass losses extend to relatively high temperatures, suggesting strong bonding between the organic fraction and other components associated with the metallic cores. In the DTA analysis, the Fe(NPs) 25% sample exhibits an exothermic peak at approximately 315 °C. The Fe(NPs) 40% sample shows two exothermic events at 245 and 326 °C, while the Fe(NPs) 50% sample displays a single exothermic peak at 375 °C. All these exothermic signals correspond to the mass losses observed in Fe(NPs) coated with guava plant extract.

The literature reports similar thermal behaviors. For example, in the green synthesis of iron nanoparticles using *Apricot kernel* peel, a thermal behavior analogous to that of the Fe(NPs) 25% sample was observed, in which Fe_3O_4 exhibited a mass loss of approximately 58%. However, this loss occurred at temperatures close to 250 °C, suggesting weaker interactions between the organic fraction and the metallic core. This loss was initially attributed to the elimination of adsorbed water and subsequently to the decomposition of organic substances [36].

In another study, iron nanoparticles were synthesized using extracts from *Daphne mezereum* leaves. Once again, the thermal behavior was similar, with mass losses occurring in two stages: the first, from room temperature to 175 °C, attributed to the loss of adsorbed water; and the second, from 175 °C to 375 °C, assigned to the decomposition of the organic fraction. The mass loss exceeded 80%, which is consistent with the results obtained for the Fe(NPs) 40% and Fe(NPs) 50% samples [37].

These thermal behaviors suggest that Fe(NPs) synthesized via green routes exhibit low thermal stability, undergoing decomposition and losing their organic fraction even at relatively low temperatures. This characteristic may represent a limitation for applications requiring high temperatures, such as sintering processes or catalytic reactions, where activity loss may occur.

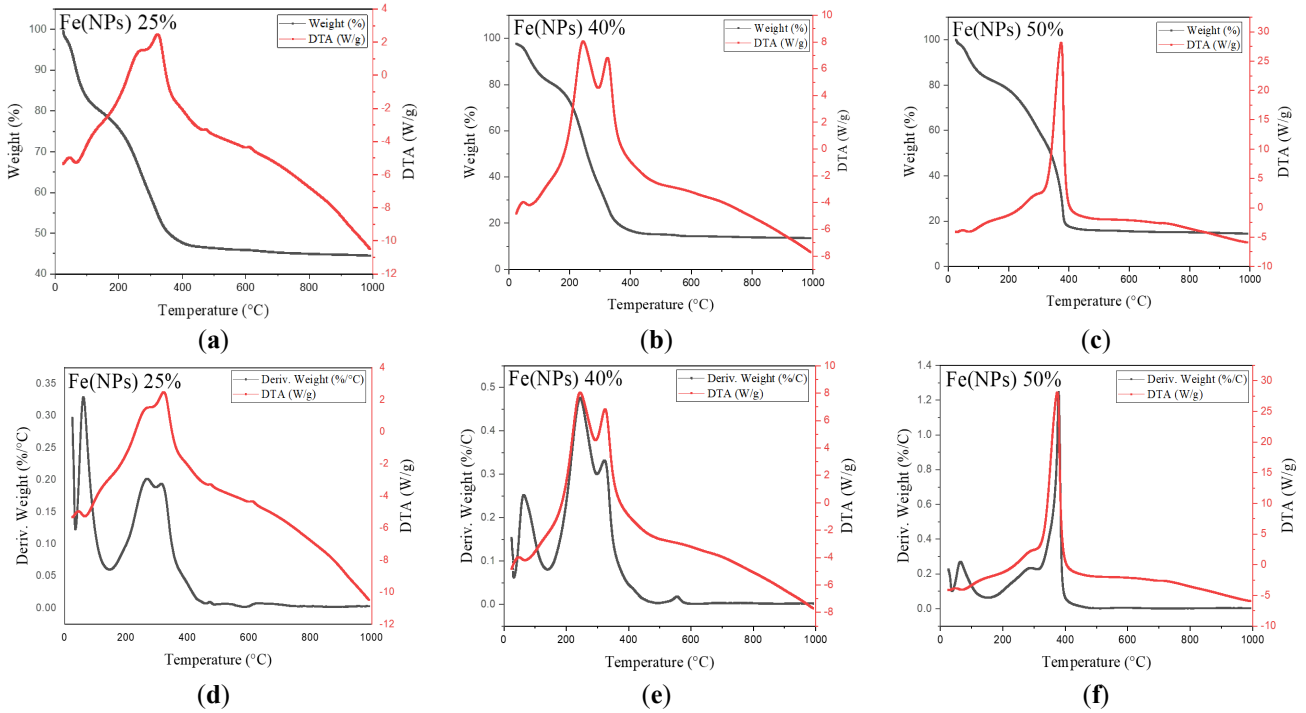

Figure 6. Thermal analysis of Fe(NPs) samples synthesized with different volumetric proportions of plant extract: Thermogravimetric analysis (TGA) and differential thermal analysis (DTA) of (**a**) Fe(NPs) 25% (**b**) Fe(NPs) 40%, and (**c**) Fe(NPs) 50%, and Derivative Thermogravimetry (DTG) and differential thermal analysis (DTA) of (**d**) Fe(NPs) 25% (**e**) Fe(NPs) 40%, and (**f**) Fe(NPs) 50%.

3.7. Catalytic Evaluation

To evaluate the catalytic performance of Fe(NPs), photocatalytic tests were conducted using 4-nitrophenol as the substrate, the Fe(NPs) as catalysts, and $NaBH_4$ as the reducing agent. Figure 7 illustrates the reaction mechanism: the gray sphere represents the Fe(NPs), the yellow circle represents 4-nitrophenolate molecules, and the blue circle represents 4-aminophenol molecules. Initially, hydrogen atoms from $NaBH_4$ molecules are adsorbed onto the catalyst surface, particularly in their porous structure, characterizing a fast and reversible process (step 1). Subsequently, 4-nitrophenolate molecules are adsorbed onto the hydrogen-rich catalyst surface in another reversible step, enabling hydrogen transfer from the catalyst to the adsorbed 4-nitrophenolate ions (step 2), resulting in the reduction to 4-aminophenol. The release of the reaction product frees the catalytic surface, allowing the catalytic cycle to restart (step 3) [38].

Additionally, according to Sravanthi (2019), $NaBH_4$ plays a crucial role as the reducing agent. Her study observed that in the absence of $NaBH_4$, conversion of 4-nitrophenol to 4-aminophenol does not occur, even after 24 h. It is important to emphasize that the presence of the catalyst is essential for accelerating the reduction process [17].

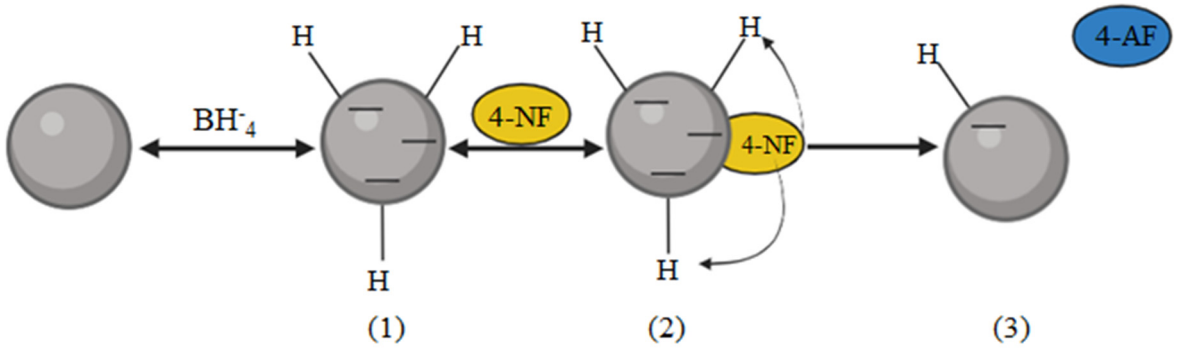

Figure 7. Illustration of the catalytic reduction mechanism of 4-nitrophenol over Fe(NPs) in the presence of $NaBH_4$.

Figure 8 presents the results obtained from the concentration of 4-nitrophenolate (C/C_0) as a function of reaction time.

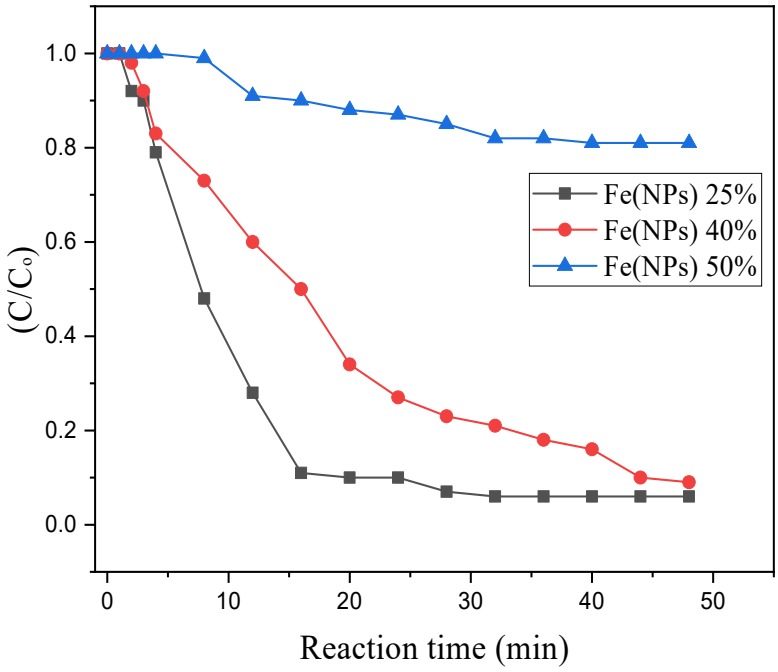

Figure 8. Concentration of 4-nitrophenolate (C/C_0) as a function of reaction time during the catalytic reduction.

Table 3 complements the results presented in Figure 8. In this context, as evidenced in a previously published study, Fe(NPs) 0%, which lacks a surface coating, exhibits the best performance, achieving complete (100%) conversion within 20 min of reaction time. Nanoparticles synthesized via chemical methods frequently display superior catalytic performance, since in green synthesis routes, the plant extract acts as a capping agent, stabilizing the nanoparticles against agglomeration. However, this coating may impact the material's reactivity by partially blocking active sites [13].

Nevertheless, Fe(NPs) 25% and Fe(NPs) 40% also demonstrated satisfactory catalytic performance, achieving 94% and 91% conversion at reaction times of 32 and 48 min, respectively. These results suggest that the coating did not significantly hinder catalytic activity in these cases. However, Fe(NPs) 50% exhibited notably lower catalytic efficiency, achieving only 19% conversion after 40 min of reaction. This reduced performance may be attributed to multiple factors, including the absence of a chemical agent in the synthesis, the larger particle size, or more pronounced surface blockage due to the higher proportion of plant extract used.

Similarly, in the study that carried out the green synthesis of iron nanoparticles using Eucalyptus leaf extract, a behavior comparable to that of Fe(NPs) 0%, Fe(NPs) 25%, and Fe(NPs) 40% was observed, with an almost complete reduction (~100%) of 4-nitrophenol to 4-aminophenol. However, as in the case of Fe(NPs) 0%, the time required for complete reduction was only 20 min [17].

In another study, iron nanoparticles and silver-iron bimetallic nanoparticles were synthesized and applied in the catalytic reduction of 4-nitrophenol. In this case, the reduction promoted by the iron nanoparticles was practically negligible. Nevertheless, upon adding silver, the reduction of 4-nitrophenol to 4-aminophenol was almost complete, reaching values close to 100% within 30 min [39]. Silver-iron bimetallic nanoparticles were also synthesized using *Calyptocarpus vialis* extract and subsequently employed in the catalytic reduction of 4-nitrophenol. In this case, a maximum conversion of 78.4% of 4-nitrophenol was achieved within 12 min [8].

These comparisons emphasize that the catalytic activity of iron nanoparticles is intrinsically related to the synthesis methods and, consequently, to their textural, morphological, and physicochemical properties. In this context, the Fe(NPs) 25% sample is noteworthy, as it exhibited a high surface area, large pore volume, good stability between the organic fraction and the metallic core, as well as the presence of organic compounds (amines, phenolics, and alcohols), which contributed both to the reduction and stabilization of the material, endowing it with excellent characteristics for application as an efficient catalyst and adsorbent. On the other hand, although the Fe(NPs) 40% sample did not display properties as prominent as those of Fe(NPs) 25%, it still demonstrated excellent catalytic performance in the reduction of 4-nitrophenol, once again suggesting a strong synergy between its properties and catalytic capacity, even under reduced $NaBH_4$ usage during the synthesis process.

Table 3. Percentage conversions relative to the reaction time required in each test.

Samples	Conversion	Reaction Time (min)
Fe(NPs) 25%	94%	32
Fe(NPs) 40%	91%	48
Fe(NPs) 50%	19%	40

A UV-Vis scan was conducted in the spectral range of 300 to 600 nm (Supplementary Material, Figure S2). $NaBH_4$ is responsible for alkalizing the reaction medium, adjusting the pH of the solution to approximately 9, which promotes the conversion of 4-nitrophenol to 4-nitrophenolate and shifts the absorption peak of the compound from 317 nm to 400 nm.

Analysis of the spectra (Figure S2) reveals a reduction in signal intensity at 400 nm, which indicates the catalytic conversion of 4-nitrophenolate over the reaction time. Notably, these decreases vary among different tests, reflecting the distinct catalytic capacities of each Fe(NPs) [40]. During the reaction process, the formation of hydrogen gas (H_2) bubbles can interfere with optical measurement and cause the loss of isosbestic points, typically reported at 280 and 314 nm [38]. Isosbestic points indicate thermodynamic conditions under which two or more phases coexist in equilibrium. Furthermore, according to Malathi (2014), the presence of the band at 360 nm is associated with the nitro (NO_2) group of the compound. A reduction in the intensity of this signal may also indicate the disappearance or reduction of the NO_2 group, and consequently, the conversion to 4-aminophenol [41].

In this context, the first-order model described by Bhole et al. (2023) was utilized to illustrate the reduction kinetics of 4-nitrophenol. This model follows the equation $\ln(C/C_0) = K_r \cdot t$, where C represents the concentration at a given time t, C_0 is the initial concentration, and K_r is the reduction rate constant [42]. Table 4 presents the reduction rate constants and determination coefficients (R^2) obtained for each Fe(NPs) sample.

Table 4. Reduction rate constants and coefficients of determination (R^2) obtained for each Fe(NPs) sample.

Samples	K_r (min^{-1})	R^2
Fe(NPs) 25%	0.10	0.97
Fe(NPs) 40%	0.05	0.99
Fe(NPs) 50%	5.8×10^{-3}	0.98

The Fe(NPs) samples fit well to the first-order model, exhibiting R^2 values ≥ 0.97. The Fe(NPs) 0% and Fe(NPs) 25% displayed the highest reduction rates, with K_r values of 0.22 and 0.1 min^{-1}, respectively [13]. Conversely, the Fe(NPs) 50% exhibited the lowest reduction rate constant, with a value of 5.8×10^{-3} min^{-1}. Thus, the first-order model demonstrated an excellent fit for the Fe(NPs) samples and confirmed that Fe(NPs) 0% and Fe(NPs) 25% exhibit the highest reduction rates.

3.8. Ecotoxicological Tests

It is worth highlighting that the results related to the samples 'BR', '$NaBH_4$', '4NF', and 'LixFe(NPs) 0%' have already been reported in previous studies and are presented again here for comparative evaluation with the other synthesized materials [13].

3.8.1. Brine Shrimp

Figure 9 shows the results of the ecotoxicological test at the trophic level of microcrustaceans.

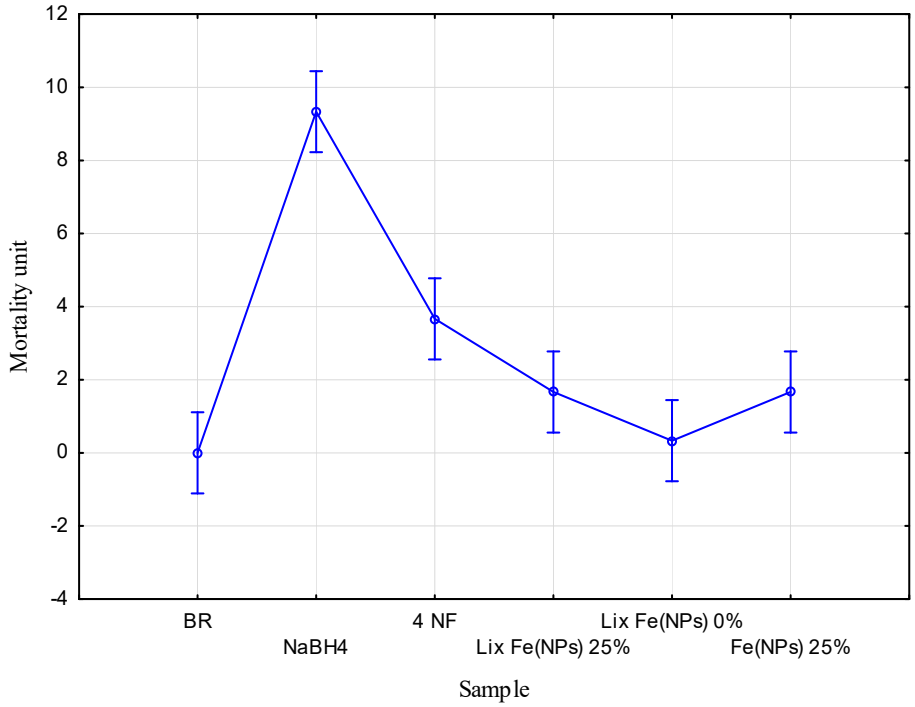

Figure 9. Ecotoxicological test at the trophic level of microcrustaceans, modified from [13].

In Figure 9, the *x*-axis represents the mean value for each sample, while the *y*-axis shows the number of deceased microcrustaceans. The Tukey test reveals statistically significant variations between samples ($p < 0.05$). To evaluate the toxicity of each sample, the effective concentration (EC_{20}) was considered, where mortality exceeding 20% (*i.e.*, 2 artemia individuals) indicates toxic effects. Accordingly, the blank sample (BR) showed no toxicity, with an average mortality of 0 individuals. Conversely, 4-nitrophenol (prior to reduction) was considered toxic, with an average mortality of approximately 3.75 microcrustaceans [13].

However, after catalytic treatment with Fe(NPs) 25%, the toxicity of the contaminant fell within the EC_{20} limit, with an average mortality of approximately 1.75 microcrustaceans. This indicates that the catalytic treatment effectively mitigated the contaminant's toxic effects.

Regarding the leachates, "Lix Fe(NPs) 25%" and "Lix Fe(NPs) 0%", exhibited average mortalities of approximately 1.75 and 0.25 individuals, respectively, remaining within non-toxic limits [13]. These results suggest that the nanomaterials possess favorable biocompatibility with organisms at this trophic level.

Finally, $NaBH_4$ exhibited high toxicity at this trophic level with an average mortality of 9 microcrustaceans, underscoring the need to explore alternative methods that minimize or replace the use of this compound [13].

3.8.2. *Lemna minor*

Figure 10 presents the ecotoxicological test results at the trophic level of aquatic plants. The *x*-axis represents the mean value for each sample, and the *y*-axis represents the variation in the number of fronds. The Tukey test reveals significant differences between samples ($p < 0.05$). To assess the toxicity of the tested samples, the effective concentration (EC_{20}) was considered, where a negative variation exceeding 20% (*i.e.*, −2 individuals) indicates toxic effects.

The blank sample (BR) showed no toxic effects, with an average variation of approximately 0.7 individuals. This suggests that, even in the absence of contaminants, *Lemna minor* did not display high clonal growth, possibly due to suboptimal temperatures during the test period. Conversely, 4-nitrophenol (4 NF) before reduction exhibited a pronounced toxic effect, with a variation of −3.75 fronds, underscoring the necessity of treatment strategies for this contaminant [13]. After catalytic reduction with Fe(NPs) 40%, the contaminant exhibited toxicity within the EC_{20} limits, with a variation of approximately −0.7 fronds. Thus, the catalytic treatment was effective in reducing the sample's toxicity.

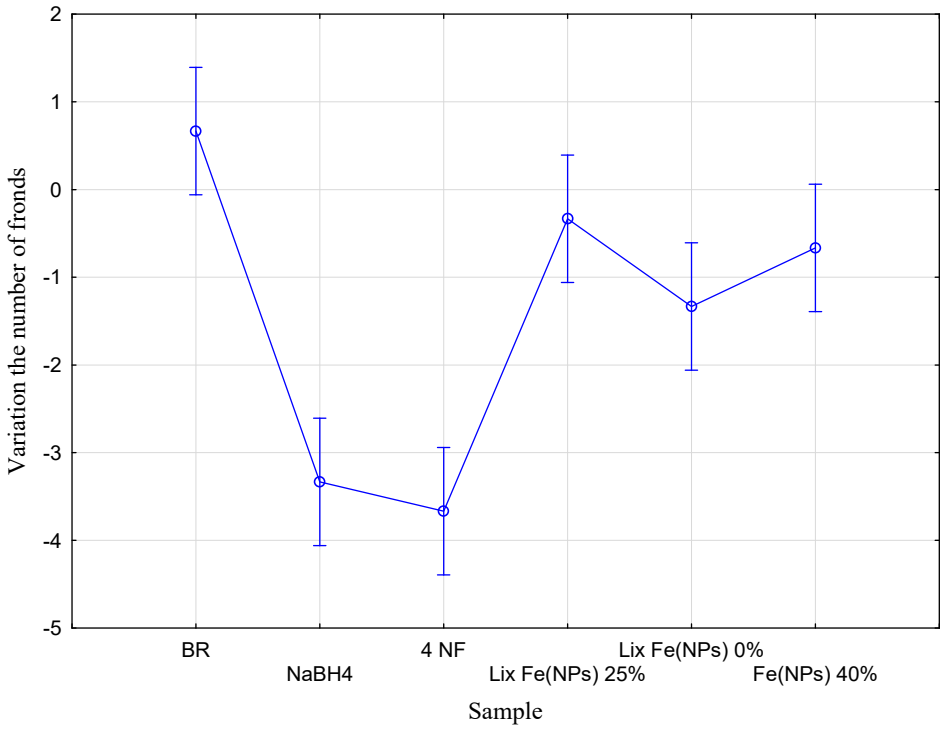

Figure 10. Ecotoxicological test at the trophic level of aquatic plants, modified from [13].

The leachates "Lix Fe(NPs) 25%" and "Lix Fe(NPs) 0%" showed variations of approximately −0.25 and −1.25 fronds, respectively [13]. Therefore, the nanomaterials demonstrated good biocompatibility with aquatic plants at this trophic level.

Finally, $NaBH_4$ exhibited high toxicity, with a variation of −3.25 fronds, exceeding the EC_{20} threshold. This underscores the need to minimize or replace the use of this compound in catalytic systems [13].

4. Conclusions

This study differs from others by employing a synthesis process that minimizes the use of the reducing agent $NaBH_4$, while simultaneously increasing the application of guava leaf aqueous extract. Furthermore, a low-cost and straightforward synthesis route was adopted, reducing the need for expensive equipment, reagents, and reaction conditions, such as controlled atmospheres and costly metals, commonly required in green synthesis processes. Notably, despite the simplicity of the procedure, it was possible to obtain highly relevant results, with catalysts exhibiting remarkable catalytic performance. For future research, modifications in the synthesis conditions are suggested, such as using controlled atmospheres, increased stirring rates, and adjustment of the $NaBH_4$ and extract addition rates. A more detailed evaluation of these parameters would enable a deeper understanding of their influence on the synthesized catalysts, particularly regarding the formation of distinct crystalline phases, textural and morphological properties and catalytic activity.

When compared to reports in the literature, the characterization of the Fe(NPs) synthesized in this study revealed notable similarities, such as the presence of iron oxides and hydroxides commonly observed in oxygenated synthesis atmospheres, reduced crystallinity in green synthesis routes, and the occurrence of organic compounds (phenols, aromatics, alcohols) acting as coating and stabilizing agents. Similar thermal behaviors were also identified, with mass loss beginning at room temperature, which may limit the catalytic applications of these materials in reactions requiring elevated temperatures. On the other hand, distinct differences were also observed, particularly for the Fe(NPs) 25%, which exhibited lepidocrocite as the sole crystalline phase and outstanding textural properties, including high surface area and pore volume, surpassing those commonly reported in the literature.

Overall, it was observed that increasing the proportion of plant extract led to the synthesis of Fe(NPs) with distinct morphological and microstructural characteristics, including lower crystallinity and reduced reactivity. These characteristics are primarily attributed to the coating effect of constituents present in the extract. Nevertheless, in the context of 4-nitrophenol reduction, reactivity assays indicated significant efficiency, even for the coated particles. Additionally, ecotoxicological tests demonstrated the biocompatibility of the treated samples and the Fe(NPs)

themselves, particularly in assays involving microcrustaceans and *Lemna minor*. Thus, Fe(NPs) synthesized with up to 40% plant extract exhibited excellent catalytic activity, being capable of reducing over 90% of 4-nitrophenol. This performance can be attributed to their favorable morphological and structural properties, as well as the stabilizing role of the plant extract. These findings underscore the potential of green-synthesized Fe(NPs) as efficient and eco-friendly catalytic agents, offering promising applications in pollutant treatment while maintaining a low environmental impact.

Supplementary Materials

The following supporting information can be found at: https://www.sciepublish.com/article/pii/714, Figure S1: Elemental mapping and EDS spectrum of Fe(NPs) synthesized with different volumetric proportions of plant extract: (a) Fe(NPs) 25%, (b) Fe(NPs) 40%, and (c) Fe(NPs) 50%; Figure S2: UV-VIS absorption spectra of catalytic reduction reactions using Fe(NPs) synthesized with: (a) Fe(NPs) 25%, (b) Fe(NPs) 40%, and (c) Fe(NPs) 50% plant extract.

Acknowledgments

The authors thank the Federal University of Technology—Paraná (UTFPR campus Pato Branco), Laboratory Central de Análises (CA), and C^{2}MMa—Centro de Caracterização Multiusuário em Pesquisa e Desenvolvimento de Materiais for the use of facilities. The authors also acknowledge the Coordination for the Improvement of Higher Education Personnel (CAPES)—Financing Code 001 for financial support.

Author Contributions

Conceptualization, F.K.d.S.N.; Methodology, F.K.d.S.N., M.B.R. and R.B.; Experimental Activities, F.K.d.S.N., M.B.R., R.B., G.G.L., Y.M.L.B. and M.A.C.d.A.; Investigation, F.K.d.S.N., M.A.C.d.A., G.G.L. and Y.M.L.B.; Resources, M.B.R. and R.B.; Data Processing and Analysis, F.K.d.S.N. and Y.M.L.B.; Writing—Original Draft Preparation, F.K.d.S.N.; Writing—Review & Editing, F.K.d.S.N., Y.M.L.B., M.B.R. and R.B.; Visualization, F.K.d.S.N.; Supervision, M.B.R. and R.B.

Ethics Statement

Not applicable.

Informed Consent Statement

Not applicable.

Data Availability Statement

The data that support the findings of this study are available from the corresponding author, Filipe Kalil da Silva Naves, upon reasonable request.

Funding

This research was funded by the Coordination for the Improvement of Higher Education Personnel (CAPES)—Finance Code 001.

Declaration of Competing Interest

The authors declare that they have no known competing financial interests or personal relationships that could have appeared to influence the work reported in this paper.

References

1. Mukherjee R, Kumar R, Sinha A, Lama Y, Saha AK. A review on synthesis, characterization, and applications of nano zero valent iron (nZVI) for environmental remediation. *Crit. Rev. Environ. Sci. Technol.* **2016**, *46*, 443–466. doi:10.1080/10643389.2015.1103832.
2. Nkosi NC, Basson AK, Ntombela ZG, Dlamini NG, Pullabhotla RV. Green synthesis and characterization of iron nanoparticles synthesized from bioflocculant for wastewater treatment: a review. *Biotechnol. Notes* **2025**, *6*, 10–31.

3. Chaudhari DS, Upadhyay RP, Shinde GY, Gawande MB, Filip J, Varma RS, et al. A review on sustainable iron oxide nanoparticles: Syntheses and applications in organic catalysis and environmental remediation. *Green Chem.* **2024**, *26*, 7579–7655. doi:10.1039/D4GC01234A.
4. Shahzadi S, Fatima S, Shafiq Z, Janjua MR. A review on green synthesis of silver nanoparticles (SNPs) using plant extracts: A multifaceted approach in photocatalysis, environmental remediation, and biomedicine. *RSC Adv.* **2025**, *15*, 3858–3903. doi:10.1039/d4ra07519f.
5. Ahmad S, Ni H, Al-Mubaddel FS, Rizk MA, Ammar MB, Khan AU, et al. Magnetic properties of different phases of iron oxide nanoparticles prepared by microemulsion-hydrothermal method. *Sci. Rep.* **2025**, *15*, 878. doi: 10.1038/s41598-025-85145-5.
6. Al-Harbi N, Abd-Elrahman NK. Physical methods for preparation of nanomaterials, their characterization and applications: a review. *J. Umm Al-Qura Univ. Appl. Sci.* **2025**, *11*, 356–377. doi:10.1007/s43994-024-00165-7.
7. Rana A, Kumari N, Tyagi M, Jagadevan S. Leaf-extract mediated zero-valent iron for oxidation of Arsenic (III): Preparation, characterization and kinetics. *Chem. Eng. J.* **2018**, *347*, 91–100. doi:10.1016/j.cej.2018.04.075.
8. Bachhar V, Joshi V, Bhatia A, Rom T, Duseja M, Shukla RK. Green synthesis of AgFe bimetallic nanoparticles from Calyptocarpus vialis plant extract for enhanced catalytic reduction of 4-nitrophenol, antioxidant, and antibacterial activities. *J. Environ. Chem. Eng.* **2025**, *13*, 116829. doi:10.1016/j.jece.2025.116829.
9. Uncu Kirtiş EB, Yiğit Koçak D, Elderviş U, Tuna S, Bayraç C. Green synthesis of iron oxide nanoparticles from extracts of Daucus carota subsp. sativus whole vegetable, peel, pomace, and juice and their application as antibacterial agents and Fenton-like catalysts. *Int. J. Food Sci. Technol.* **2025**, *60*, vvae035.
10. Joga SB, Korabandi D, Lakkaboyana SK, Kumar V. Synthesis of iron nanoparticles on lemon peel carbon dots (LP-CDs@Fe_3O_4) applied in photocatalysis, antioxidant, antidiabetic, and hemolytic activity. *Inorg. Chem. Commun.* **2025**, *174 P1*, 113960. doi:10.1016/j.inoche.2025.113960.
11. Archana V, Joseph PJ, Kalainathan S. Simple One-Step Leaf Extract-Assisted Preparation of α-Fe_2O_3 Nanoparticles, Physicochemical Properties, and Its Sunlight-Driven Photocatalytic Activity on Methylene Blue Dye Degradation. *J. Nanomater.* **2021**, *2021*, 8570351. doi:10.1155/2021/8570351.
12. Puthukkara AR, Jose TS, Dinoop S. Plant mediated synthesis of zero valent iron nanoparticles and its application in water treatment. *J. Environ. Chem. Eng.* **2021**, *9*, 104569. doi:10.1016/j.jece.2020.104569.
13. Naves FKS, Bueno YML, Rocha RDC, Brackmann R, Rodrigues MB. Green synthesis of iron nanoparticles (Fe(NPs)) using plant extract from Eucalyptus grandis: characterization and determination of the catalytic potential for reduction of 4-nitrophenol. *Rev. Ambient. Água.* **2024**, *19*, e2978. doi:10.4136/ambi-agua.2978.
14. Shahid A, Muhamma I, Muhammad R, Beenish I. Phytochemical screening and in vitro radical scavenging activities of "Gola" guava fruit and leaf extracts. *J. Food Process. Preserv.* **2022**, *46*, e16989. doi:10.1111/jfpp.16989.
15. Samari F, Salehipoor H, Eftekharb E, Yousefinejad S. Low-temperature biosynthesis of silver nanoparticles using mango leaf extract: Catalytic effect, antioxidant properties, anticancer activity and application for colorimetric sensing. *New J. Chem.* **2018**, *42*, 15905–15916. doi:10.1039/c8nj03156h.
16. Amezquita-Garcia HJ, Rangel-Mendez JR, Cervantes FJ, Razo-Flores E. Bioreactors packed with activated carbon fibers as redox mediators in the anaerobic biotransformation of 4-Nitrophenol to 4-Aminophenol. *Bol. Grupo Esp. Carbón* **2017**, *3*, 15–17.
17. Sravanthi K, Ayodhya D, Swamy PY. Green synthesis, characterization and catalytic activity of 4-nitrophenol reduction and formation of benzimidazoles using bentonite supported zero valent iron nanoparticles. *Mater. Sci. Energy Technol.* **2019**, *2*, 298–307. doi:10.1016/j.mset.2019.02.003.
18. Díaz-de-Cerio E, Vito V, Ana María G, Alberto F, Antonio S. Determination of polar compounds in guava leaves infusions and ultrasound aqueous extract by HPLC-ESI-MS. *J. Chem.* **2015**, *2015*, 250919. doi:10.1155/2015/250919.
19. Dong H, Zhao F, Zeng G, Tang L, Fan C, Zhang L, et al. Aging study on carboxymethyl cellulose-coated zero-valent iron nanoparticles in water: Chemical transformation and structural evolution. *J. Hazard. Mater.* **2016**, *312*, 234–242. doi:10.1016/j.jhazmat.2016.03.069.
20. Dong H, Zhao F, He Q, Xie Y, Zeng Y, Zhang L, et al. Physicochemical transformation of carboxymethyl cellulose-coated zero-valent iron nanoparticles (nZVI) in simulated groundwater under anaerobic conditions. *Sep. Purif. Technol.* **2017**, *175*, 376–383. doi:10.1016/j.seppur.2016.11.053.
21. Singh H, Desimone MF, Pandya S, Jasani S, George N, Adnan M, et al. Revisiting the green synthesis of nanoparticles: uncovering influences of plant extracts as reducing agents for enhanced synthesis efficiency and its biomedical applications. *Int. J. Nanomed.* **2023**, *18*, 4727–4750. doi:10.2147/IJN.S419369.
22. Bibi I, Nazar N, Ata S, Sultan M, Ali A, Abbas A, et al. Green synthesis of iron oxide nanoparticles using pomegranate seeds extract and photocatalytic activity evaluation for the degradation of textile dye. *J. Mater. Res. Technol.* **2019**, *8*, 6115–6124. doi:10.1016/j.jmrt.2019.10.006.
23. Adhikari A, Chhetri K, Acharya D, Pant B. Adhikari A. Green Synthesis of Iron Oxide Nanoparticles Using Psidium. *Catalysts* **2022**, *12*, 1188. doi:10.3390/catal12101188.

24. Sun Y, Li X, Zhang W, Wang HP. A method for the preparation of stable dispersion of zero-valent iron nanoparticles. *Colloids Surf. A Physicochem. Eng. Asp.* **2007**, *308*, 60–66. doi:10.1016/j.colsurfa.2007.05.029.
25. Singh G, Jalandhara D, Yadav K. Effect of grain size on optical properties of iron oxide nanoparticles. *AIP Conf. Proc.* **2016**, *1728*, 020409. doi:10.1063/1.4946460.
26. Casassa-Padrón AM, Portillo E, González C. FTIR-ATR for the identification of Psidium guajava plants infested with Meloidogyne enterolobii. *Rev. Fac. Agron.* **2022**, *39*, 2. doi:10.47280/RevFacAgron(LUZ).v39.n3.03.
27. Karu E, Magaji B, Mohammed Bello A. Green synthesis, spectroscopic analysis and stabilization energy of iron oxide nanoparticles from aqueous Ziziphus leaf extract. *Bima J. Sci. Technol.* **2022**, *6*, 40–49.
28. Kumari T, Phogat D, Shukla V. Exploring the multipotentiality of plant extracts for the green synthesis of iron nanoparticles: A study of adsorption capacity and dye degradation efficiency. *Environ. Res.* **2023**, *229*, 116025. doi:10.1016/j.envres.2023.116025.
29. Mokshith DG, Kalpashree MM, Krishna DK. Natural Synthesis of Nanoparticles using Flower Extract of Hymenocallis littoralis (Jacq) Salisb and Evaluation of its Antimicrobial activity. *Int. J. Res. Appl. Sci. Eng. Technol.* **2022**, *10*, 1199–1207. doi:10.22214/ijraset.2022.47158.
30. Kharisov B, Kharissova OV, Dias HVR, Méndez UO, Fuente IG, Peña Y, et al. Iron-based nanomaterials in the catalysis. In *Advanced Catalytic Materials—Photocatalysis and Other Current Trends*; InTech: Rijeka, Croatia, 2016; pp. 1–36. doi:10.5772/61862.
31. Amos-Tautua BM, Fakayode OJ, Songca SP, Oluwafemi OS. Effect of synthetic conditions on the crystallinity, porosity and magnetic properties of gluconic acid capped iron oxide nanoparticles. *Nano-Struct. Nano-Objects* **2020**, *23*, 100480. doi:10.1016/j.nanoso.2020.100480.
32. Fekry M, Shafek SH, Soliman FS, Bakry A. Impact of poly naphthalene sulfonate on the dispersion stability of iron oxide nanoparticles. *Egypt. J. Petrol.* **2023**, *32*, 23–32. doi:10.1016/j.ejpe.2023.01.001.
33. Atran AA, Ibrahim FA, Awwad NS, Hamdy MS. Iron incorporated porous cerium oxide nanoparticles as an efficient photocatalyst for different hazardous elimination. *J. Rare Earths* 2024, 43, 726-735. doi:10.1016/j.jre.2024.02.006.
34. Sirdeshpande KD, Sridhar A, Cholkar KM, Selvaraj R. Structural characterization of mesoporous magnetite nanoparticles synthesized using the leaf extract of Calliandra haematocephala and their photocatalytic degradation of malachite green dye. *Appl. Nanosci.* **2018**, *8*, 675–683. doi:10.1007/s13204-018-0698-8.
35. Wang Q, Kanel SR, Park H, Ryu A, Choi H. Controllable synthesis, characterization, and magnetic properties of nanoscale zerovalent iron with specific high Brunauer–Emmett–Teller surface area. *J. Nanopartic. Res.* **2009**, *11*, 749–755.
36. Ben Kouider T, Souli L, Derouiche Y, Soltani T, Maschke U. Green synthesis and characterization of Fe_3O_4 and ε-Fe_2O_3 nanoparticles using apricot kernel shell extract and study of their optical properties. *Physchem* **2025**, *5*, 33. doi:10.3390/physchem5030033.
37. Beheshtkhoo N, Kouhbanani MA, Savardashtaki A, Amani AM, Taghizadeh S. Green synthesis of iron oxide nanoparticles by aqueous leaf extract of Daphne mezereum as a novel dye-removing material. *Appl. Phys. A Mater. Sci. Process.* **2018**, *124*, 363. doi:10.1007/s00339-018-1782-3.
38. Wunder S, Lu Y, Albrecht M, Ballauff M. Kinetic analysis of catalytic reduction of 4-nitrophenol by metallic nanoparticles immobilized in spherical polyelectrolyte brushes. *J. Phys. Chem. C* **2010**, *114*, 8814–8820. doi:10.1021/jp101125j.
39. Chiou JR, Lai BH, Hsu KC, Chen DH. One-pot green synthesis of silver/iron oxide composite nanoparticles for 4-nitrophenol reduction. *J. Hazard. Mater.* **2013**, *248–249*, 394–400. doi:10.1016/j.jhazmat.2013.01.030.
40. Biswas S, Pal A. Iron oxide-loaded alginate-bentonite hydrogel beads as a green and sustainable catalyst for 4-nitrophenol reduction. *Mater. Today Commun.* **2021**, *28*, 102588. doi:10.1016/j.mtcomm.2021.102588.
41. Malathi S, Ezhilarasu T, Abiraman T, Balasubramanian S. One pot green synthesis of Ag, Au and Au–Ag alloy nanoparticles using isonicotinic acid hydrazide and starch. *Carbohydr. Polym.* **2014**, *111*, 734–743. doi:10.1016/j.carbpol.2014.04.105.
42. Bhole R, Gonsalves D, Murugesan G, Narasimhan MK, Srinivasan NR, Dave N, et al. Superparamagnetic spherical magnetite nanoparticles: synthesis, characterization and catalytic potential. *Appl. Nanosci.* **2023**, *13*, 6003–6014. doi:10.1007/s13204-022-02532-4.